Chemical Engineering Journal 359 (2019) 344–353

Contents lists available at ScienceDirect

Chemical Engineering Journal

journal homepage: www.elsevier.com/locate/cej

Economical synthesis strategy of RHO zeolites with fine-tuned composition and porosity for enhanced trace CO_2 capture

Quanli Ke[a,b], Tianjun Sun[a,*], Xiaoli Wei[a,b], Ya Guo[a,b], Shutao Xu[a,*], Shudong Wang[a,*]

[a] Dalian National Laboratory for Clean Energy, Dalian Institute of Chemical Physics, Chinese Academy of Sciences, Dalian 116023, China
[b] University of Chinese Academy of Sciences, Beijing 100049, China

HIGHLIGHTS

- Cesium-crown ether complexes were the key structure-directing agents of RHO zeolite.
- Synthesis cost was greatly reduced by substitution of the Cs^+ by cheaper K^+ cations.
- Different $K^+/Na^+/Cs^+$ ratios could generate diverse silica contents in RHO zeolites.
- Medium-silica RHO zeolites achieve fine trade-off for adsorption heat and capacity.
- Medium-silica RHO zeolites retain high selectivities for ultralow binary mixtures.

GRAPHICAL ABSTRACT

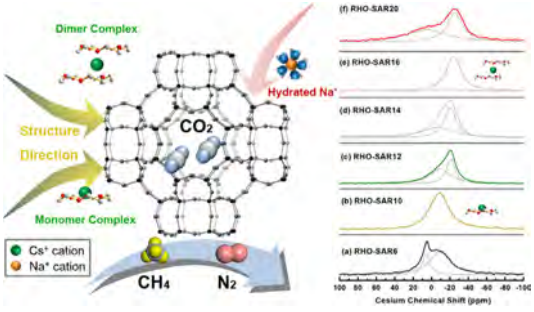

ARTICLE INFO

Keywords:
Silica content control
Alkali metal cations
Crown ether
Carbon dioxide capture
Zeolites

ABSTRACT

Delicate modification of the silica contents and porous structures within RHO zeolites has been readily realized by adopting a variety of alkali metal-crown ether (AMCE) complexes as the templates. Compared to the previous protocols, up to 70% of the Cs^+ cations could be substituted by much cheaper K^+ cations and thus the synthesis costs of RHO zeolites could be impressively reduced. The subsequent ^{133}Cs and ^{23}Na MAS NMR spectra further reveal that the Cs^+ cations may aggregate with crown ether in a form of monomer or dimer complex, which then plays a significant role in the structural direction of RHO zeolites, whereas the hydrated Na^+ cations mainly serve as the charge balancing cations. Meanwhile, the addition of different amount of K^+ cation could result in varying degrees of template-framework interaction and consequently generates RHO zeolites with diverse compositions. Finally, the proton-type RHO zeolites were applied to the adsorptive separation of $CO_2/CH_4/N_2$ mixture. Therein, the medium-silica ones achieve fine trade-off for the adsorption capacity, selectivity and heat even under ultralow CO_2 concentration, which makes them potential candidates for trace CO_2 capture.

1. Introduction

Recent years have witnessed the widespread applications of supramolecular chemistry in processes such as selective separation, asymmetric catalysis, material technology and drug delivery [1–5]. Conceptually, supramolecules refer to those complexes constructed by two or more molecules via noncovalent interactions like van der Waals forces, hydrogen bonding, metal coordination and hydrophobic forces [6,7]. The self-assembly, folding, molecular recognition, host-guest chemistry among the supramolecules have imparted them unique

* Corresponding authors.
E-mail addresses: suntianjun@dicp.ac.cn (T. Sun), xushutao@dicp.ac.cn (S. Xu), wangsd@dicp.ac.cn (S. Wang).

https://doi.org/10.1016/j.cej.2018.11.098
Received 13 August 2018; Received in revised form 30 October 2018; Accepted 13 November 2018
Available online 13 November 2018
1385-8947/

spatial arrangements, electrostatic affinity and hydrophilic/hydrophobic characters [8]. Taking advantages of these distinct properties, the supramolecules could play a significant role in the synthesis of a series of functionalized zeolites, including high-silica, extra-large-pore, hierarchical and enantioselective zeolites, as well as the zeolite frameworks with *in-situ* incorporation of transition metal cations [9–13].

Macrocycles are frequently adopted as the building blocks in supramolecular systems, of which the cavities could react easily with guest molecules. As a typical macrocycle, crown ether can aggregate with various alkali metal cations (Li^+, Na^+, K^+, Cs^+, etc.) and form AMCE complexes with diverse spatial conformations [14–16]. Employing the AMCE complexes as the organic structure-directing agents (OSDA), a variety of high-silica zeolites, including topologies of FAU, RHO, KFI and MSO, could be readily synthesized [17–20]. The framework of RHO zeolite is comprised of a cubic stacking of LTA cages connected by double-eight-member (D8R) rings. Our previous publications have revealed the structure-directing role of a special cesium-crown ether complex, which could remarkably promote the silica contents within the framework of RHO zeolite [21,22]. However, two defects are still remaining in the preparation of RHO zeolites: one is the silica-alumina ratio (SAR) gap between the conventional RHO zeolite (SAR ≈ 6) and the reported high-silica RHO zeolite (SAR ≈ 16), which would ultimately restrict the potential applications of RHO zeolites to adsorption and catalytic processes; the other one is the relatively high synthesis expense, especially the cost of the indispensable Cs^+ cation. During the adsorption process, the SAR value of zeolite adsorbent is intimately associated with its electric field intensity, which would then exert significant but exactly opposite influence on the adsorption capacity and adsorption heat; consequently, either a too high or too low SAR value would be adverse for the zeolite adsorbent to achieve a fine trade-off between the adsorption property and regenerability [23–25]. To fill in the SAR gap, we intend to modify the interaction between the AMCE complexes and zeolite frameworks by delicately adjusting the concentrations as well as chemical compositions of the AMCE complexes, and thus adapting their overall charge density. In the meantime, the possibility of lowering the manufacture cost of RHO zeolite could also be explored by directly decreasing or partially substituting the Cs^+ amounts during the synthesis.

In this paper, the controllable synthesis of RHO zeolites with consecutively increasing SAR values has been realized by careful modification of the AMCE complex compositions. Compared to the former recipe, up to 70% of the Cs^+ cation amounts could be substituted by K^+ cation; in contrast, only 20% of the cesium amounts could be spared when the diluted AMCE complexes were directly taken as the OSDA. The subsequent NMR spectra disclose that it is the coordination state between the Cs^+ cation and crown ether molecules that plays a vital role in the structural orientation of the RHO zeolites, while the hydrated Na^+ cations chiefly serve as the charge compensating cations. In this consideration, varying amounts of K^+ cations were then added to adjust the chemical composition and charge density of the AMCE complex because of its intermediate interaction with both water and crown ether molecules. Afterwards, the trace CO_2 removal performances were tested on the proton-type RHO zeolites with varying SAR values. Since our previous research has already revealed the strong water resistance of the proton-type RHO zeolites, here we primarily concentrate on the enhancement of their adsorptive properties. According to the adsorption isotherms, the medium-silica RHO zeolites show the highest capacities and selectivities toward CO_2. The IAST calculations were further conducted to simulate their binary gas adsorption behaviors. Likewise, the medium-silica zeolites exhibit excellent adsorption performances even under CO_2 concentration as low as 1%. This point not only indicates that the manufacture costs and adsorption efficiencies of RHO zeolites might be simultaneously optimized, but also provides a promising strategy for versatile zeolite synthesis via the crown ether-based supramolecular chemistry.

2. Experimental

2.1. Chemical and materials

18-crown-6 (TCI; > 98%), sodium hydroxide (Kermel; > 96%), cesium hydroxide (J&K chemical; 50% aqueous, > 99%), potassium hydroxide (SCR Co. Ltd; > 85%), sodium aluminate (SCR Co. Ltd; > 41% Al_2O_3), sodium fluoride (Tianjin Guangfu; > 98%), Ludox AS-40 (Aldrich; 40 wt%, suspension in water), NH_4Cl (Kermel; > 99.5%). All chemicals of analytical grade were used without further purification.

2.2. Preparation of the organic directing agent (OSDA)

The AMCE complex series were prepared on the basis of our previous publication [21]. 5.3 g of 18-crown-6 was dissolved in 3.5 g of distilled water. Then 0.7 g of sodium hydroxide and 2.0 g of cesium hydroxide were added to the solution mentioned above, and the resulting mixture was stirred with reflux at 353 K for 3 h. Thereafter a mixture with two visible phases was obtained. The supernatant of this mixture was taken out and denoted as AMCE-2 complex because the ratio between the 18-crown-6 and cesium ion in its chemical composition is about 2. Thereafter, the initial ratios between the 18-crown-6 and cesium ion were changed to 4 and 8 and the reductive parts of cesium cations were substituted by equimolar amounts of potassium cations. After reactions under the same conditions, the supernatants of the resultant mixtures were taken out and denoted as AMCE-4 and AMCE-8 complex, respectively. The TAMCE complex was also prepared according to the former research [18]. 2.6 g of 18-crown-6, 1.3 g of sodium hydroxide and 2.0 g of cesium hydroxide were dissolved in 18.0 g of distilled water. The resulting mixture was stirred at 353 K for 3 h. Only a clear solution without stratification was obtained, and denoted as TAMCE complex.

2.3. Syntheses of RHO zeolites via AMCE-2 complex

As referred to our previous research, several high-silica RHO zeolites were synthesized by the adoption of AMCE-2 complex as the OSDA [21]. 0.7 g of sodium aluminate were first dissolved in 6.6 g of distilled water along with 100 mg RHO zeolite seeds. The mixture above was fully stirred and then transferred into a closed polytef bottle containing 9.0 g of the AMCE-2 complex. Subsequently, 8.45 g of colloidal silica, Ludox AS-40, were added into the polytef bottle and the resulting reaction mixture was stirred continuously at room temperature for 24 h. The crystallization was carried out in Teflon-lined stainless steel autoclaves at 413 K under rotation for 6 days. The synthesized zeolites were denoted as RHO-SAR14 according to the chemical composition analyses. After reaction, the solid obtained was filtered, washed with distilled water then dried at 373 K overnight, and finally calcined at 823 K for 6 h in order to remove the occluded organic material. When 0.56 g and 0.467 g of sodium aluminate were added instead, both along with 0.05 g addition of sodium fluoride, the silica contents within the product zeolites were also changed. In this regard, the as-synthesized zeolites were denoted as RHO-SAR16 and RHO-SAR20, respectively, according to their chemical compositions. Both zeolites were treated next by the same processes.

2.4. Syntheses of RHO zeolites via AMCE-4 and AMCE-8 complexes

0.7 g of sodium aluminate were first dissolved in 6.6 g of distilled water along with 100 mg RHO zeolite seeds. The mixture above was fully stirred and then transferred into a closed polytef bottle containing 9.6 g of the AMCE-4 or AMCE-8 complex. Subsequently, 8.45 g of colloidal silica, Ludox AS-40, were added into the polytef bottle and the resulting reaction mixture was stirred continuously at room temperature for 24 h. The crystallization was carried out in Teflon-lined stainless steel autoclaves at 413 K under rotation for 6 days. The synthesized

zeolites were denoted as RHO-SAR12 and RHO-SAR10, which correspond to the employment of the AMCE-4 or AMCE-8 complex, respectively. After reaction, the solids obtained were filtered, washed with distilled water then dried at 373 K overnight, and finally calcined at 823 K for 6 h in order to remove the occluded organic material.

2.5. Syntheses of conventional RHO-SAR6 via TAMCE complex

As a benchmark, RHO-SAR6 was synthesized according to a published procedure of Chatelain [18] The TAMCE complex (aq) was first transferred into a closed polytef bottle. Subsequently, 30.0 g of colloidal silica, Ludox AS-40, was also added into the polytef bottle and the resulting reaction mixture was stirred continuously at room temperature for 24 h. The crystallization was carried out in Teflon-lined stainless steel autoclaves at 383 K under rotation for 4 days. The synthesized zeolites were denoted as RHO-SAR6 according to the chemical composition analyses. After reaction, the solids obtained were filtered, washed with distilled water then dried at 373 K overnight, and finally calcined at 823 K for 6 h in order to remove the occluded organic material.

2.6. Ion exchange details of the synthesized zeolites

The ammonium ion exchanges of the synthesized zeolites were first conducted to remove the bulky metal cations within the zeolites. The calcined zeolites were exchanged with 6 mol/L NH_4Cl solution (5 ml/g zeolite) four times at 353 K each for 1 h. The obtained NH_4-exchanged zeolites were then calcined under 873 K for more than 6 h to get the corresponding H-form zeolites.

2.7. Characterizations

The characterizations of synthesized RHO zeolites include PXRD, TGA, ICP, FE-SEM, EDS, NMR and physical ad-sorption isotherm. Powder X-ray data were collected on a Panalytical X'Pert PRO diffractometer with Bragg-Brentano geometry, using Cu Kα radiation. The patterns were obtained from 5 to 50° (2θ) using a step size of 0.02° (2θ) and 0.267 s per step. ICP-AES analyses were conducted on PerkinElmer Optima8x00. Thermogravimetric analyses (TGA) were recorded on a Netzsch STA449F3 instrument from 30 °C to 1000 °C, at a heating rate of 5 °C/min in air flow, using ceramic pan. The morphology and elemental compositions of RHO zeolites were obtained by field emission scanning electron microscopy (FE-SEM) on a Jeol JSM-7800F electron microscope equipped with an Oxford energy dispersive X-ray spectroscopy (EDX). Solid-state ^{29}Si, ^{27}Al MAS NMR spectra were performed on Bruker Avance III 500 spectrometer using a 4 mm MAS probe. The resonance frequencies were 99.36 and 130.32 MHz for ^{29}Si and ^{27}Al, respectively. Deconvolution of ^{29}Si Solid-state MAS NMR spectroscopy, in which all aluminum occupies tetrahedral sites, was used to determine the framework Si/Al ratios of RHO zeolites [26]. Solid-state ^{133}Cs, ^{23}Na and 2D MQ ^{23}Na MAS NMR were performed on Bruker Avance III 600 spectrometer using a 3.2 mm MAS probe. The resonance frequencies were 78.71 and 158.75 MHz for ^{133}Cs and ^{23}Na, respectively. Two dimension (2D) ^{23}Na multiple-quantum (MQ) MAS NMR experiments were applied to RHO-SAR20, RHO-SAR16, RHO-SAR14 and RHO-SAR6 in order to obtain the precise information about the coordination states of the sodium cation within the zeolite channels. A two-dimensional (2D) Fourier transformation followed by a shearing transformation gave a pure absorption mode 2D contour plot [27]. Argon adsorption isotherms in the pressure range of 0–1 bar were measured on a Quantachrome Autosorb-iQ2 instrument. All the samples were evacuated at 573 K for 12 h under dynamic vacuum prior to analysis. The textual properties of all the samples were then obtained from the adsorption isotherms. The linearity of fitting for the Brunauer-Emmett-Teller (BET) specific surface area (S_{BET}) was 0.99999; Total pore volume (V_t) was calculated by Gurvich-rule at $P/P^0 = 0.95$; Micropore volume (V_{mic}) and micropore surface area (S_{mic}) were calculated by t-Plot method; Pore size distributions (PSDs) of all the samples were calculated by SF method since the micropores were dominant in all the samples.

2.8. The adsorption experiments

The carbon dioxide, methane and nitrogen single component adsorption were measured on Quantachrome Autosorb-iQ2 at 288, 298 and 308 K over a pressure range of 0–100 kPa. The instrument was equipped with a Polyscience AD07R-20-AA2Y recirculating thermostatic bath for precise temperature control. All the adsorption data were fitted using the Langmuir-Freundlich (L-F) model. The ideal selectivity (Henry's law selectivity) was defined as the ratio of Henry's law constants of single gas component which are calculated from the Langmuir-Freundlich equation. At low partial pressure range, the equilibrium selectivity could be estimated as the ratio of the Henry's law constants, which is just the case of carbon capture from dilute-purity sources. To further predict the adsorption behavior of zeolites for binary gas mixtures, the IAST model was employed herein since collection of experimental data for a gas mixture was neither convenient nor rapid. Finally, the isosteric heat of adsorption (Q_{st}) of CO_2 on different RHO zeolites could be determined from the Clausius-Clapeyron equation, applying the Langmuir-Freundlich fits for adsorption isotherms at different temperatures. Furthermore, the heat of adsorption at zero coverage can be determined from Henry's law constants according to the van't Hoff equation.

3. Results and discussion

3.1. Characterizations of RHO zeolites with varying SAR values

Our former researches have shown that the adoption of cesium cation is quite essential to the synthesis of high-silica RHO zeolite, which in turn brings out the problem of manufacture costs [21,22]. Two solutions were then put forward to address this dilemma: one is the decrease of the absolute amount, or concentration, of the AMCE complex; another is the substitution of the Cs^+ cation in the synthesis gel by much cheaper K^+ cation. Basing upon the previously reported protocols, several diluted AMCE complexes have been applied to the RHO zeolite synthesis as the OSDAs (Section 1.2). According to the XRD patterns in Fig. S2.1, the RHO zeolites were synthesized only if the concentrations of the AMCE complex were higher than 80 wt%, which means that the manufacture expense could not be significantly reduced by this method. In this circumstance, we attempted to replace the Cs^+ cations in the synthesis gels by equimolar K^+ cations to maintain the whole quantity of the positive ions (Section 1.3). In this way, a range of RHO zeolites have been successfully synthesized wherein up to 70% of the Cs^+ amount within the AMCE complexes could be substituted, even lower than the amount adopted in conventional protocol (Fig. 1A, Table 1). Notably, the crystallinity of the RHO zeolites observed in the XRD patterns varied along with the crown ether/Cs^+ ratios. As demonstrated by the FE-SEM images of the as-synthesized zeolites, the crystallinity of RHO-SAR20 and RHO-SAR6 was comparatively weaker than the other zeolites, which coincides well with the organic weight loss in the TGA curves (Fig. 1B, Fig. 2). Furthermore, this phenomenon reveals that the replacement of the Cs^+ cations in the AMCE complexes by K^+ cations would not interfere with the crystallization of RHO zeolites and hence the purpose to cut down the synthesis expense could be well achieved by this means.

Normally, the variation of alkali metal cations within the AMCE complex might change its overall charge density and thus influence its interaction with the zeolite frameworks [28]. In this respect, the framework silica contents of the as-prepared RHO zeolites were then estimated by the combination of the ^{29}Si MAS NMR spectra, ICP-AES and EDX analyses (Fig. 1C, Table S2.1). The ^{29}Si MAS NMR spectra in Fig. 1C primarily include four various signals, $Q^4[Si(OSi)_4]$, Si(1Al)[Si

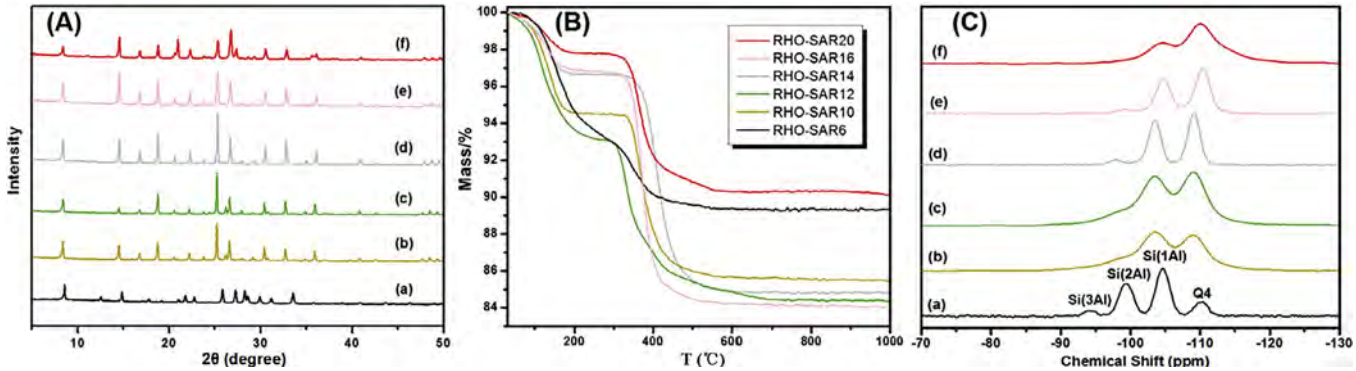

Fig. 1. (A) XRD patterns, (B) Thermogravimetric weight loss and (C) ^{29}Si MAS NMR spectra patterns of the as-prepared RHO zeolites with increasing SAR values: (a) RHO-SAR6 (black), (b) RHO-SAR10 (golden), (c) RHO-SAR12 (green), (d) RHO-SAR14 (grey), (e) RHO-SAR16 (pink) and (f) RHO-SAR20 (red). (For interpretation of the references to colour in this figure legend, the reader is referred to the web version of this article.)

Table 1
Textural Properties of H-form RHO Zeolites with Different Silica-alumina Ratios.

Adsorbents	$(Cs^+/Silica)_{gel}$	S_{BET}	S_{mic}	V_t	V_{mic}
		$(m^2\,g^{-1})$	$(m^2\,g^{-1})$	$(cm^3\,g^{-1})$	$(cm^3\,g^{-1})$
H-RHO-SAR20	0.12	336	308	0.157	0.110
H-RHO-SAR16	0.12	803	746	0.338	0.259
H-RHO-SAR14	0.12	934	903	0.364	0.316
H-RHO-SAR12	0.09	981	957	0.362	0.333
H-RHO-SAR10	0.04	897	872	0.334	0.302
H-RHO-SAR6	0.06	699	663	0.295	0.236

$(OSi)_3(OAl)_1]$, Si(2Al)$[Si(OSi)_2(OAl)_2]$, Si(3Al) $[Si(OSi)_1(OAl)_3]$ [29]. The deconvolutions of the ^{29}Si MAS NMR spectra give framework SAR values of 25.6, 17.7, 13.8, 12.8, 11.0 and 6.2 for RHO-SAR20, RHO-SAR16, RHO-SAR14, RHO-SAR12, RHO-SAR10 and RHO-SAR6, respectively (Fig. S2.2–2.7, Table S2.1), just lying within the optimum SAR value range for carbon capture [23]. On the other hand, the SAR values obtained from the ICP-AES and EDX analyses were 21.3, 16.5, 13.7, 12.0, 9.8 and 5.6 for the corresponding zeolites, which were highly consistent with the deconvolution results (Table S2.1). Additionally, the ^{27}Al NMR spectra of all the zeolites show only one sharp signal centered around 60 ppm, which suggests that little extraframework alumina species are present and thus the alumina species should be mostly incorporated into the zeolite frameworks (Fig. S2.8). The values in the zeolite denotations were also derived from the ICP-AES and EDX results. Coincident with our expectations, the silica contents within the zeolite frameworks could be fine-tuned by carefully adjusting the chemical compositions of the AMCE complexes and thus the SAR gap existing in the RHO zeolites was validly fixed.

3.2. Synthesis mechanism of RHO zeolites

In order to explore the role the AMCE complex plays during the synthesis, the ^{133}Cs MAS NMR spectra were subsequently collected for the as-synthesized RHO zeolites (Fig. 3). The assignments of the ^{133}Cs MAS NMR signals and their parameters have been summarized in Table S2.2. Accordingly, three different resonance peaks, namely SI, SII and SIII, have been detected after decomposition of the NMR spectra.

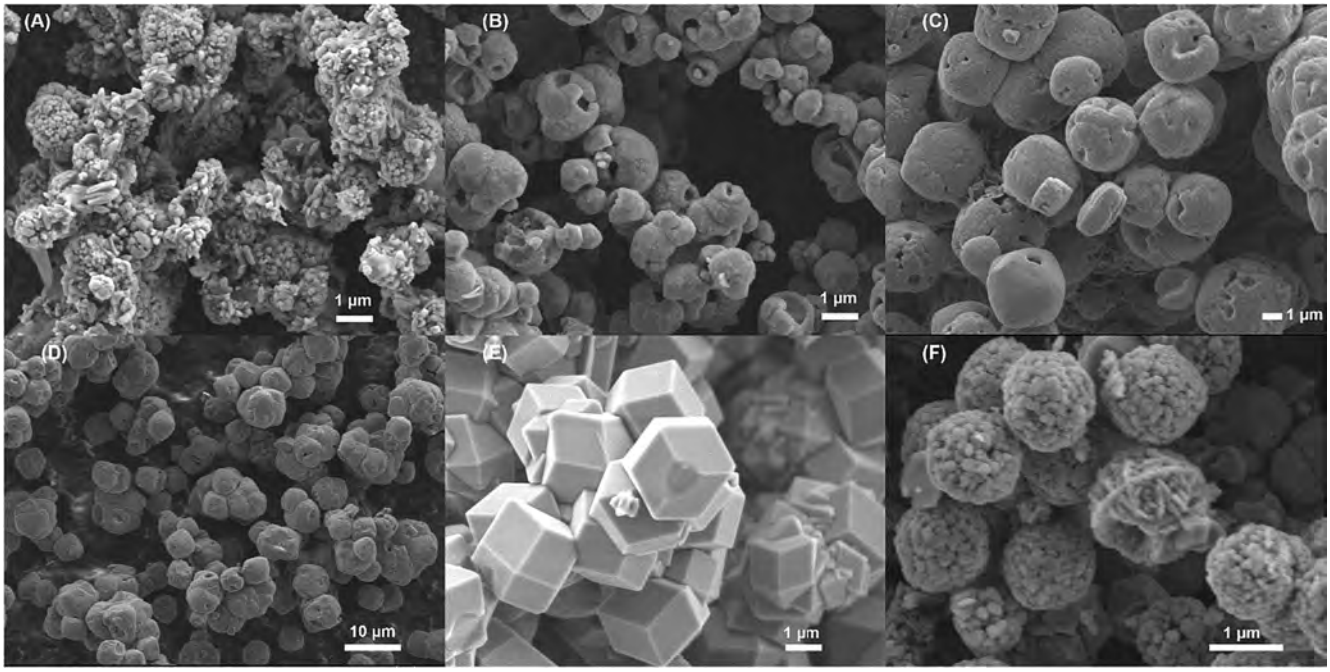

Fig. 2. SEM images of the as-prepared RHO zeolites: (A) RHO-SAR20, (B) RHO-SAR16, (C) RHO-SAR14, (D) RHO-SAR12, (E) RHO-SAR10 and (F) RHO-SAR6, the SAR values in the names were derived from the ICP and EDX results.

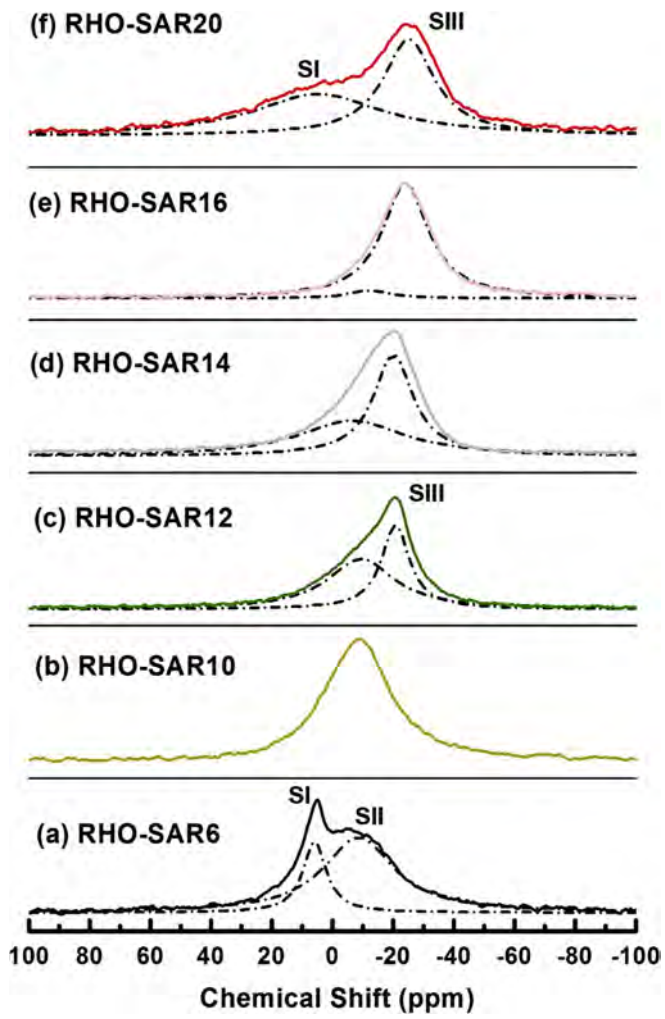

Fig. 3. ^{133}Cs MAS NMR spectra of the as-made RHO zeolites with increasing SAR values: (a) RHO-SAR6 (black), (b) RHO-SAR10 (golden), (c) RHO-SAR12 (green), (d) RHO-SAR14 (grey), (e) RHO-SAR16 (pink) and (f) RHO-SAR20 (red). The assignment of the signals and the NMR parameters are given in Table S2.2, the black dash lines refer to the deconvolutions of the spectra. (For interpretation of the references to colour in this figure legend, the reader is referred to the web version of this article.)

Because of the small quadrupole moment of the ^{133}Cs nuclei, the quadrupolar coupling influence could be neglected for the cesium-containing zeolites [30,31]. In this case, the presence of three different signals in the ^{133}Cs MAS NMR spectra actually indicates three distinct local environments for the cesium species. As referred to the literatures, the resonance position of SI at ca. 4.6 and 5.9 ppm should be attributed to the fully hydrated Cs^+ cations (Fig. 4) [32]. Furthermore, although the exact assignments have not been hitherto clarified, the SII and SIII signals should be irrelevant to the exchanged Cs^+ cations at the active sites or the extraframework cesium species [33–35]. Meanwhile, it has been manifested that the chemical shift of Cs^+ cation would migrate to a more negative value as its coordination number increases [36]. This point, when combined with the simultaneous growth of the SAR values and the SIII signal fractions in the ^{133}Cs MAS NMR spectra (Fig. 3, Table S2.2), strongly confirms that the high coordination state of the Cs^+ cation would benefit the enhancement of silica contents within the RHO zeolites. Our previous publications have suggested the key impact of the cesium-crown ether dimer complex in guiding the formation of high-silica RHO zeolites [21]. Given this, we then ascribe the resonance positions of SII and SIII to the cesium-crown ether monomer and dimer complex (Fig. 4), respectively, which is in agreement with the UV–vis

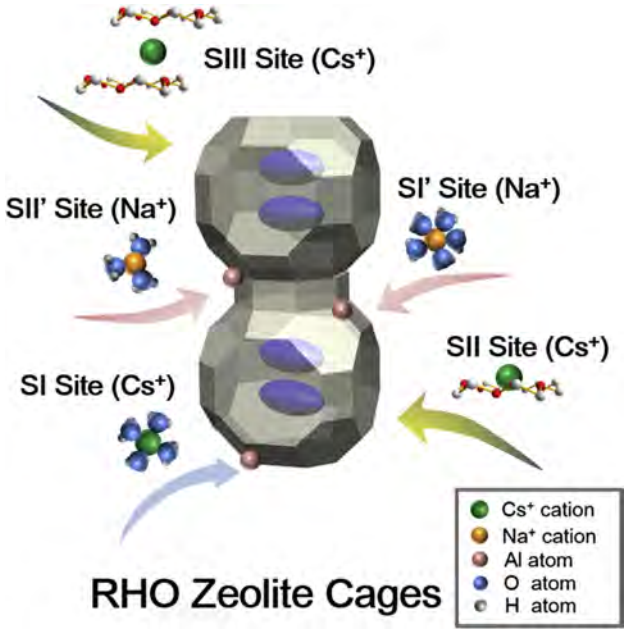

Fig. 4. Schematic description for the assignments of resonance peaks in the ^{133}Cs and ^{23}Na MAS NMR spectra of the as-made RHO zeolites. (SI: fully hydrated Cs^+ cation, SII: Cs^+-crown ether monomer complex, SIII: Cs^+-crown ether dimer complex; SI': fully hydrated Na^+ cation, SII': partially hydrated Na^+ cation.)

spectra and chemical composition analyses in the aforementioned study [21].

To further investigate the synthesis mechanism, the ^{23}Na MAS NMR and the two-dimensional multiple-quantum (MQ) MAS NMR were performed on RHO-SAR6, RHO-SAR14, RHO-SAR16 and RHO-SAR20 to exclude the influence of K^+ cations therein. As seen in Fig. 5, the ^{23}Na MAS NMR spectra could all be sorted into two types of resonance peaks, SI' and SII'. The former signal, close to 0 ppm, has been proven to be related to the fully hydrated Na^+ cation, while the latter one, observed round −7 ppm, should be attributed to the partially hydrated Na^+ cation in simultaneous interaction with the oxygen belonging to the zeolite framework (Fig. 4) [37,38]. The hydrated state of the Na^+ cation would also be rationalized by its significantly high hydration energy, which results in the prior coordination of residual water in the AMCE complexes with Na^+ rather than Cs^+ (Table S2.3). Meanwhile, given the high affinity between the crown ether molecules and alkali metal cations (Table S2.3), it is logical to consider that any crown ether molecules existing in the AMCE complexes should be tightly associated with certain alkali metal cations, particularly the Cs^+ cations according to our assumption. Then the synthesis mechanism could be well interpreted: Na^+ would be first hydrated by the residual water in the AMCE complexes and later serves as the charge compensating cation; on the other hand, Cs^+ aggregates with the crown ether molecules to form a variety of cesium-crown ether complexes, monomer or dimer. Counting on the intermediate affinity of K^+ with both water and crown ether (Table S2.3), the addition of different amount of K^+ cations would result in diverse distribution of the monomer and dimer, which further leads to varying degrees of template-framework interaction and finally generates RHO zeolites with different levels of silica contents (Fig. 3, Table S2.2). That means, the K^+ cations actually serve as the buffering ions in the gel when facing the competition between Na^+ and Cs^+ cations. Noticeably, two samples show exceptional properties in this process: the ^{133}Cs MAS NMR spectrum of RHO-SAR6 is constituted of resonance peaks at SI and SII, which suggests the co-template effects of the hydrated Cs^+ cation as well as the cesium-crown ether monomer complex; additionally, the SI signal could also be detected in the ^{133}Cs MAS NMR spectrum of RHO-SAR20, which should be connected to the

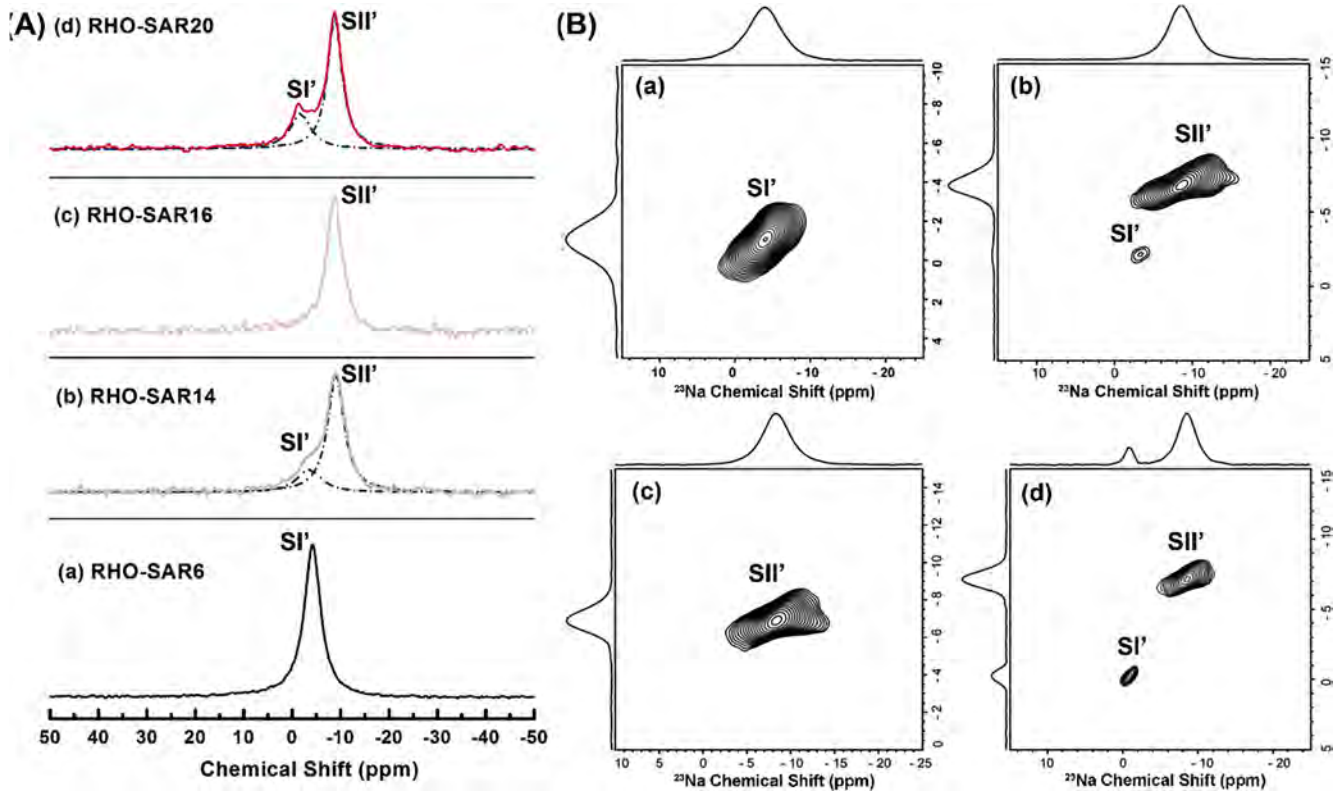

Fig. 5. (A) ^{23}Na MAS NMR spectra and (B) two-dimensional multiple-quantum (MQ) ^{23}Na MAS NMR of the as-made RHO zeolites with increasing SAR values (a) RHO-SAR6 (black), (b) RHO-SAR14 (grey), (c) RHO-SAR16 (pink) and (d) RHO-SAR20 (red). The assignment of the signals and the NMR parameters are given in Table S2.2, the blue dash lines refer to the deconvolutions of the spectra. (For interpretation of the references to colour in this figure legend, the reader is referred to the web version of this article.)

incomplete crystallization derived from the insufficient alumina contents in the gel (Fig. 2). The porous structures and adsorption properties of these two zeolites would both be affected in this situation, which is discussed in the following section.

3.3. Carbon capture on H-RHO zeolites with varying SAR values

After verifying the synthesis mechanism, we then apply the synthesized RHO zeolites to the carbon capture process. Provided the high polarity of CO_2 and its strong interaction with zeolite frameworks, the regenerability and the energy consumption should be an unneglectful factor. Typically, the energy penalty for regeneration is deeply influenced by the interaction between the electric field of cations and the adsorbates [23–25,39]. In this consideration, proton was chosen as the charge balancing cation instead of metal cations in order to weaken the field potential of the RHO zeolites, given the severe shielding effect on the electric field by the short distances between framework oxygen and hydrogen atoms ($d_{O\text{-}H} \approx 1$ Å) [24]. The total energy involved in a physical adsorption process could be described as the sum of following interaction items:

$$\varphi = \varphi_D + \varphi_R + \varphi_{Ind} + \varphi_{F\mu} + \varphi_{FQ} + \varphi_{sp}$$

where the six items represent, correspondingly, dispersion energy, repulsion energy, induction energy, field-dipole energy, field gradient-quadrupole interaction and adsorbate-adsorbate interaction [24].

The single-component adsorption isotherms were first taken in order to examine the adsorption properties of the H-RHO zeolites for varying adsorbates. The adsorption pressure range was set between 0 and 100 kPa, which was in accordance with the conditions adopted by vacuum swing adsorption process [24,40]. In addition, carbon capture under ambient conditions would be of great advantages in commercial applications because of its low energy demand [23]. As shown in Fig. 6A–C, the adsorption capacities on each H-RHO sample decrease in the sequence of $CO_2 \gg CH_4 > N_2$. The higher uptake of CH_4 than that of N_2 on each zeolite should be mainly caused by its larger polarizability, while the especially large adsorption capacity of CO_2 ought to be attributed to its small molecular dimension (σ) and consequently high accessibility and pore-filling effect within the zeolite channels (Table S3.1). It should also be noted that the adsorption capacities on the H-RHO zeolites yield a volcano-type growth as the SAR values increase, wherein the medium-silica RHO zeolites show the largest capacities for CO_2, CH_4 and N_2 (Fig. 8A, Table 2). Notably, the optimum gas adsorption capacities were obtained when the AMCE-4 complex was adopted as the template. In consideration that RHO zeolites could only be synthesized within certain range of Cs^+ concentration (Fig. S2.9), it could then be concluded that there should exist an optimum 18-crown-6/Cs^+ ratio in the initial reactant gel.

Basically, the six potential terms mentioned above, within the physical adsorption range, primarily depend on two elements, the pore size and the field intensity [41–43]. As demonstrated in Fig. 6E, little discrepancies have been detected in the pore size distributions of the H-RHO zeolites. In contrast, the electric potential within the zeolites is reversely proportional to the SAR values of the zeolites, which leads to the preferable adsorption on low-silica zeolites [23–25,41]. The surface areas and pore volumes are also crucial for the adsorption results. With this regard, the argon adsorption-desorption isotherms were then measured at 87 K to investigate the pore structures of the H-RHO zeolites with varying silica contents (Fig. 6D). Obviously, micropores are predominant in all the H-RHO zeolites (Fig. 6D, Table 1). Besides, the porous parameters of the H-RHO zeolites also yield a volcano-type distribution versus their SAR values. The inferior porosity of H-RHO-SAR20 should be attributed to the destabilization effect of the negatively charged siloxy defects on the zeolite framework or the nuclei, which arises from the deficiency of alumina species [44–46]. As for the

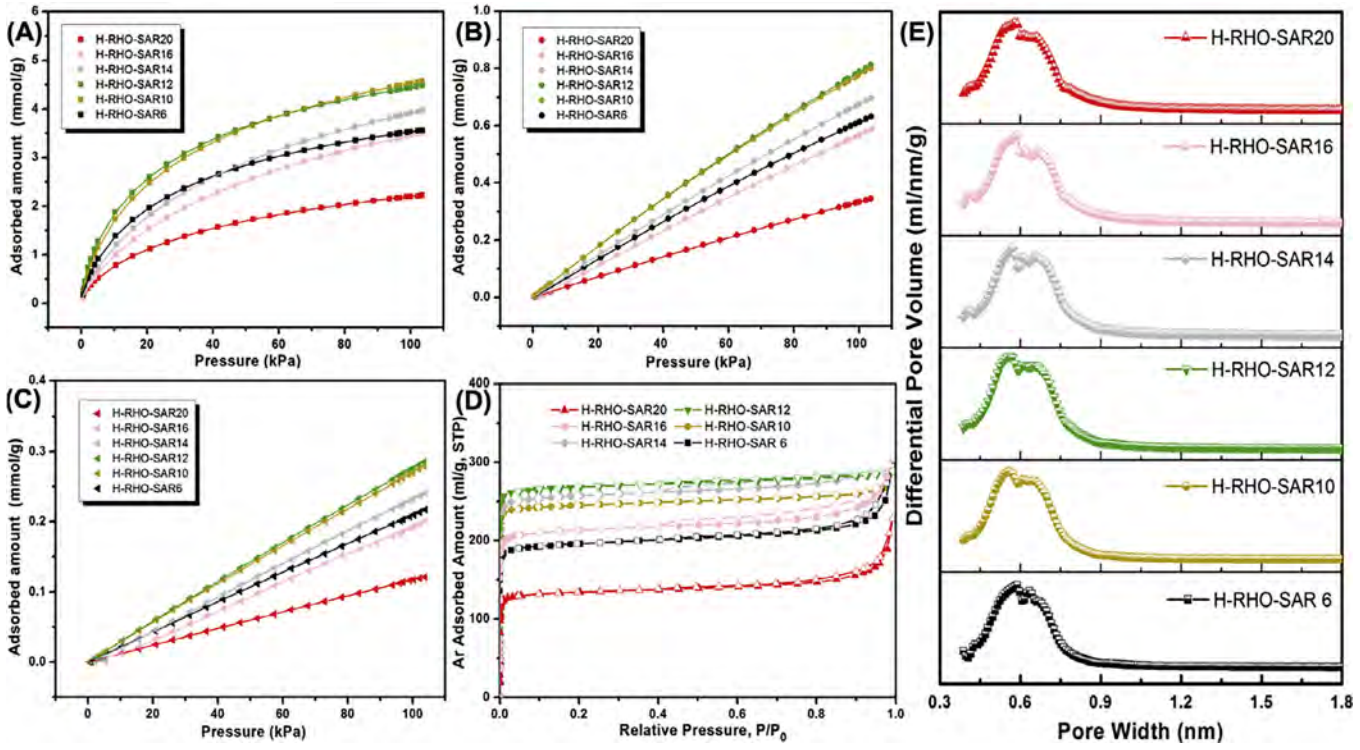

Fig. 6. (A) CO_2 adsorption isotherms, (B) CH_4 adsorption isotherms and (C) N_2 adsorption isotherms of H-RHO-SAR6 (black), H-RHO-SAR10 (golden), H-RHO-SAR12 (green), H-RHO-SAR14 (grey), H-RHO-SAR16 (pink) and H-RHO-SAR20 (red) at 298 K, the solid lines were data simulated by Langmuir-Freundlich equation, the linearity of fitting is 0.999. (D) Argon adsorption - desorption isotherms at 87 K and (E) Pore size distributions (PSD) obtained from argon adsorption - desorption isotherms of H-RHO-SAR6 (black), H-RHO-SAR10 (golden), H-RHO-SAR12 (green), H-RHO-SAR14 (grey), H-RHO-SAR16 (pink) and H-RHO-SAR20 (red). (For interpretation of the references to colour in this figure legend, the reader is referred to the web version of this article.)

other five H-RHO zeolites, their porosity difference should also be closely associated with the different chemical compositions of their organic templates, which could result in varying degrees of template-framework interaction and consequently generate RHO zeolites with diverse pore structures [28,47]. Combining the textural parameters of the zeolites with their corresponding adsorption behaviors, it could then be concluded that the adsorptive capacities of the zeolites get enhanced concurrently with the increase of surface areas and pore volumes (Tables 1 and 2). This conclusion further verifies the strong interaction between the pore walls and the nonpolar adsorbates, especially for the CO_2 molecule (0.33 nm) which could interact simultaneously with both the side-walls inside the appropriate pore openings of the RHO zeolites (0.5–0.6 nm) [48,49]. Eventually, the conflicting effects of the electric field and pore walls come to a compromise and give rise to the convex tendency of the adsorptive amounts as well as the CO_2 working capacities versus the SAR value increments, wherein the most optimum SAR value range is within 10–14 (Fig. 8A).

The trace CO_2 removal is of prime priority in diverse feedstock prepurification processes such as air separation and alkaline fuel cell [50,51]. In order to simulate the trace CO_2 removal processes, we then conduct the IAST calculations on different zeolites for two gas mixtures, CO_2/CH_4 and CO_2/N_2, each with CO_2 concentrations of 1%. Noticeably, the accuracy of the IAST calculation has been previously confirmed on various zeolitic types toward a mass of binary gas mixtures [52,53]. With the total pressure increases, the CO_2/CH_4 and CO_2/N_2 adsorptive selectivities on all of the H-RHO zeolites decline simultaneously, as attributed to the gradual coverage of the active sites within the zeolites (Fig. 7A and B). Furthermore, the selectivity slopes for CO_2/CH_4 binary gas mixture always decrease in the following order: H-RHO-SAR10 (and 20) > H-RHO-SAR6 (and 12) > H-RHO-SAR14 (and 16) (Fig. 7A). This result fit well with their adsorption isotherms above, which once again verify the high affinity toward CO_2 while excluding CH_4 on the medium-silica H-RHO zeolites. The same trends have also been observed for the CO_2/N_2 binary gas mixture but with greatly higher selectivity values, which should be ascribed to the much lower affinity toward N_2 on all the H-RHO zeolites (Fig. 7B). Interestingly, the IAST selectivities for both binary gas systems on H-RHO-SAR20 are particularly high among all the zeolites. This phenomenon is possibly associated with the inferior adsorption for N_2 on H-RHO-SAR20, as originated from the weak electric field within this zeolite as well as its low surface area and pore volume (Table 1). Ultimately, the Henry selectivities were compared to the IAST predicted selectivities at 298 K and 1 bar on zeolites with increasing SAR values (Table 2). Most of the selectivity values estimated from both methods are in high coincidence except for the case of H-RHO-SAR16, of which the residual stress derived from the framework defects should be responsible [22]. Besides, in a view of high CO_2 selectivity over the other gases, the most appropriate SAR value range for carbon capture should be located within 6 to 12 (Fig. 8B). Taking both the adsorption capacity and selectivity into the account, the breakthrough experiments were further conducted over H-RHO-SAR10 and H-RHO-SAR12 to investigate their separation performances under dynamic conditions (Figs. S3.7–S3.8). The results show that both CH_4 and N_2 gases break much more quickly than CO_2, which once again verifies the high binary selectivity of both H-RHO zeolites even under CO_2 concentration as low as 1%.

Basing upon the single component adsorption isotherms at different temperatures, the isosteric heats of adsorption (Q_{st}) for CO_2 were then estimated by the Clausius-Clapeyron equation and plotted against the CO_2 loadings (Fig. 7C). Similar to the IAST calculation results, the Q_{st} values of CO_2 also drop gradually because of the accumulated consumption of the active sites or framework defects. More specifically, the isosteric heats of adsorption at zero coverage could be calculated through the van't Hoff equation on the basis of Henry's law constants (Table 2). Generally, the isosteric heats toward CO_2 are found approximate on H-RHO zeolites with varying SAR values. Moreover, when compared with other conventional zeolitic types, all the H-RHO zeolites

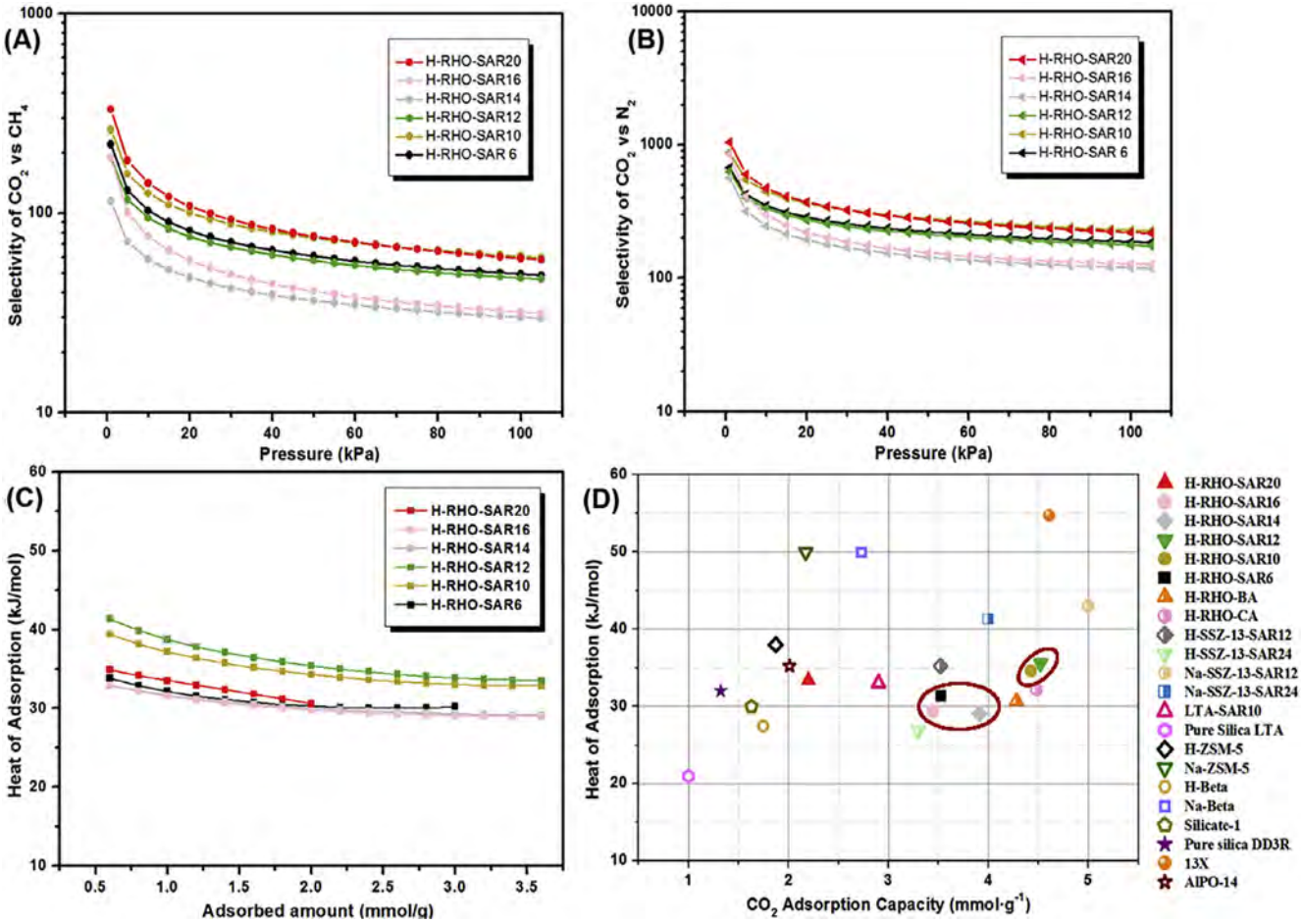

Fig. 7. (A) The IAST predicted selectivities toward CO_2/CH_4 (1:99) mixtures at 298 K, (B) The IAST predicted selectivities toward CO_2/N_2 (1:99) mixtures at 298 K and (C) Heat of adsorption for CO_2 on H-RHO-SAR6 (black), H-RHO-SAR10 (golden), H-RHO-SAR12 (green), H-RHO-SAR14 (grey), H-RHO-SAR16 (pink) and H-RHO-SAR20 (red). (D) The summarization of the isosteric heat of adsorption toward CO_2 on some conventional zeolites versus their CO_2 loadings at 298 K and 1 bar. (The zeolites in the red circles refer to those synthesized in this paper; see more details in Tables S3.5 and S3.6.) (For interpretation of the references to colour in this figure legend, the reader is referred to the web version of this article.)

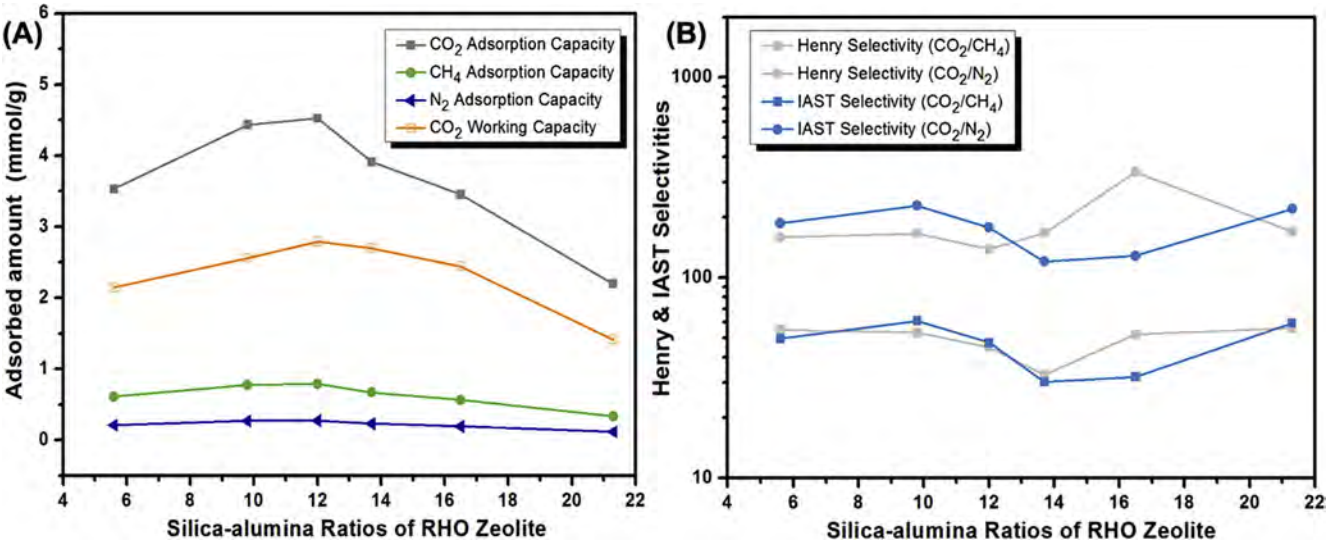

Fig. 8. (A) The changes of gas loadings as well as CO_2 working capacities and (B) the variations of the Henry selectivity as well as IAST predicted selectivities versus the SAR values increments of the H-RHO zeolites.

Table 2
The Adsorption Parameters for CO_2, CH_4 and N_2 on H-RHO Zeolites with Different Silica-alumina Ratios at 298 K.

Adsorbent	Adsorption Capacity at 1 bar (mmol g^{-1})			Henry Selectivity for binary gases at 298 K		IAST Selectivity for binary gases at 298 K and 1 bar		Working Capacity (mmol g^{-1})[a]	ΔH^0_{iso} (kJ·mol^{-1})[b]
	CO_2	CH_4	N_2	CO_2/CH_4	CO_2/N_2	CO_2/CH_4	CO_2/N_2	CO_2	CO_2
H-RHO-SAR20	2.20	0.33	0.12	56	170	59	220	1.41	33.4
H-RHO-SAR16	3.45	0.57	0.19	52	337	32	128	2.44	29.4
H-RHO-SAR14	3.91	0.67	0.23	33	167	30	120	2.70	29.1
H-RHO-SAR12	4.52	0.79	0.28	45	139	47	178	2.79	35.6
H-RHO-SAR10	4.43	0.77	0.27	53	166	61	229	2.56	34.6
H-RHO-SAR6	3.53	0.61	0.21	55	159	50	187	2.14	31.3

[a] Measured as (Uptake at 1 bar – Uptake at 0.1 bar).
[b] Determined from Henry's law constants according to the van't Hoff equation.

synthesized in this paper, except the H-RHO-SAR20, could achieve considerable adsorption capacities while retaining relatively lower adsorption heat for CO_2 (Fig. 7D). This trade-off between the isosteric heat and adsorption capacity makes the H-RHO zeolites synthesized here the excellent candidates for carbon capture process. Along with the increase of the CO_2 uptakes, all the isosteric heat values finally come to convergences but are still much larger than those obtained on the pure-silica zeolites (Fig. 7C, Tables S3.5 and S3.6). In this circumstance, neither the attraction of the active sites nor the gas-gas interaction would be the dominant force anymore [23]. As deduced from the adsorption results, the electrostatic force of the framework and the molecule-pore wall interaction constitute the two primary but conflicting forces during the adsorption process. Lobo et al. have also revealed the strong appeal of the pore wall to the adsorbate molecules at the eight-membered-ring (8MR) sites within the microporous zeolites [54,55]. Then the isosteric adsorption heats on different H-RHO zeolites at high loadings could be illuminated: the approximate adsorption heat values of the zeolites should be originated from their adjacent pore size distributions, wherein the higher Q_{st} values of the H-RHO-SAR10 (and 12) than those of H-RHO-SAR14 (and 16) are likely to be caused by the relatively stronger electrostatic fields in the former two zeolites, while the intermediate Q_{st} values of the H-RHO-SAR6 and H-RHO-SAR20 may have strong connection to their weak crystallinity and massive framework defects, respectively. In an overall view, however, the medium-silica RHO zeolites (H-RHO-SAR10 and 12) should have advantages over the other ones when the adsorption capacity, binary selectivity and isosteric heats were all taken into account.

4. Conclusions

As described, a series of RHO zeolites with increasing silica contents have been synthesized under the guidance of different AMCE complex templates. By partially substituting the Cs^+ cations within the AMCE complex by inexpensive K^+ cations, the manufacture expenses could be greatly reduced when compared to the conventional synthesis protocol. To further investigate the synthesis mechanism, the ^{133}Cs MAS NMR spectra and the ^{23}Na MQ MAS NMR spectra were collected on all the synthesized zeolites. According to the signal assignments, the high coordination state of Cs^+ cation, quite probably in a form of cesium-crown ether dimer complex, is evidently beneficial to the enhancement of silica contents within zeolites. Meanwhile, the Na^+ cations were hydrated first and the bulky hydrated ions served as the charge balancing cations thereafter. Different amounts of K^+ cations were then added to the gel to carefully adjust the chemical composition and overall charge density of the AMCE complex. In this manner, the interaction between the zeolite frameworks and AMCE complexes could also be modified which thus affects the incorporation of alumina species. Finally, the H-form RHO zeolites were applied to the adsorptive separation of CO_2, CH_4 and N_2, wherein the medium-silica RHO zeolites may have advantages over their analogues for the balance they achieve for working capacity, selectivity and adsorption heat. Moreover, the ideal adsorbed solution theory (IAST) predictions indicate that the medium-silica RHO zeolites could exhibit high selectivities toward CO_2/CH_4 and CO_2/N_2 binary mixtures even under 1% CO_2 concentrations, which gives them great potential for trace CO_2 removal processes. Notably, this work provides a promising way to modify the silica contents within zeolite frameworks and may shed light upon a broader application of crown ether-based supramolecular chemistry to the synthesis of other zeolite topologies such as FAU in the future.

Acknowledgment

This work was supported by grants from the National Natural Science Foundation of China (No. 21776266 and 21476231).

Declarations of interest

None.

Appendix A. Supplementary data

Supplementary data to this article can be found online at https://doi.org/10.1016/j.cej.2018.11.098.

References

[1] M.J. Webber, E.A. Appel, E.W. Meijer, R. Langer, Supramolecular biomaterials, Nat. Mater. 15 (2016) 13–26.
[2] R. Arletti, E. Fois, L. Gigli, G. Vezzalini, S. Quartieri, G. Tabacchi, Irreversible conversion of a water-ethanol solution into an organized two-dimensional network of alternating supramolecular units in a hydrophobic zeolite under pressure, Angew. Chem. Int. Ed. 56 (2017) 2105–2109.
[3] K.M. Wenz, G. Leonhardt-Lutterbeck, B. Breit, Inducing axial chirality in a supramolecular catalyst, Angew. Chem. Int. Ed. 57 (2018) 5100–5104.
[4] G. Li, J. Shang, Q.F. Gu, R.V. Awati, N. Jensen, A. Grant, X.Y. Zhang, D.S. Sholl, J.Z. Liu, P.A. Webley, E.F. May, Temperature-regulated guest admission and release in microporous materials, Nat. Commun. 8 (2017).
[5] Y.Z. Wang, O. Zeiri, M. Raula, B. Le Ouay, F. Stellacci, I.A. Weinstock, Host-guest chemistry with water-soluble gold nanoparticle supraspheres, Nat. Nanotechnol. 12 (2017) 170–176.
[6] H.J. Schneider, Binding mechanisms in supramolecular complexes, Angew. Chem. Int. Ed. 48 (2009) 3924–3977.
[7] F. Biedermann, H.J. Schneider, Experimental binding energies in supramolecular complexes, Chem. Rev. 116 (2016) 5216–5300.
[8] G.V. Oshovsky, D.N. Reinhoudt, W. Verboom, Supramolecular chemistry in water, Angew. Chem. Int. Ed. 46 (2007) 2366–2393.
[9] A. Corma, F. Rey, J. Rius, M.J. Sabater, S. Valencia, Supramolecular self-assembled molecules as organic directing agent for synthesis of zeolites, Nature 431 (2004) 287–290.
[10] M. Choi, H.S. Cho, R. Srivastava, C. Venkatesan, D.H. Choi, R. Ryoo, Amphiphilic organosilane-directed synthesis of crystalline zeolite with tunable mesoporosity, Nat. Mater. 5 (2006) 718–723.
[11] F.J. Chen, Y. Xu, H.B. Du, An extra-large-pore zeolite with intersecting 18-, 12-, and 10-membered ring channels, Angew. Chem. Int. Ed. 53 (2014) 9592–9596.
[12] R. Martínez-Franco, M. Moliner, P. Concepcion, J.R. Thogersen, A. Corma, Synthesis, characterization and reactivity of high hydrothermally stable Cu-SAPO-34 materials prepared by "one-pot" processes, J. Catal. 314 (2014) 73–82.
[13] S.K. Brand, J.E. Schmidt, M.W. Deem, F. Daeyaert, Y.H. Ma, O. Terasaki, M. Orazov,

M.E. Davis, Enantiomerically enriched, polycrystalline molecular sieves, Proc. Natl. Acad. Sci. U.S.A. 114 (2017) 5101–5106.
[14] E.D. Glendening, D. Feller, M.A. Thompson, An ab-initio investigation of the structure and alkali-metal cation selectivity of 18-crown-6, J. Am. Chem. Soc. 116 (1994) 10657–10669.
[15] A.A. Al-Kahtani, N.A. Al-Jallal, A.A. El-Azhary, Conformational and vibrational analysis of 18-crown-6-alkali metal cation complexes, Spectrochim. Acta A Mol. Biomol. Spectrosc. 132 (2014) 70–83.
[16] H.R. Yu, J.Q. Hu, X.H. Lu, X.J. Ju, Z. Liu, R. Xie, W. Wang, L.Y. Chu, Insights into the effects of 2:1 “sandwich-type” crown-ether/metal-ion complexes in responsive host-guest systems, J. Phys. Chem. B 119 (2015) 1696–1705.
[17] F. Delprato, L. Delmotte, J.L. Guth, L. Huve, Synthesis of new silica-rich cubic and hexagonal faujasites using crown-ether-based supramolecules as templates, Zeolites 10 (1990) 546–552.
[18] T. Chatelain, J. Patarin, E. Fousson, M. Soulard, J.L. Guth, P. Schulz, Synthesis and characterization of high-silica zeolite RHO prepared in the presence of 18-crown-6 ether as organic template, Micropor. Mater. 4 (1995) 231–238.
[19] T. Chatelain, J. Patarin, R. Farre, O. Petigny, P. Schulz, Synthesis and characterization of 18-crown-6 ether-containing KFI-type zeolite, Zeolites 17 (1996) 328–333.
[20] D.F. Shantz, A. Burton, R.F. Lobo, Synthesis, structure solution, and characterization of the aluminosilicate MCM-61: the first aluminosilicate clathrate with 18-membered rings, Micropor. Mesopor. Mater. 31 (1999) 61–73.
[21] Q. Ke, T. Sun, H. Cheng, H. Chen, X. Liu, X. Wei, S. Wang, Targeted synthesis of ultrastable high-silica RHO zeolite through alkali metal-crown ether interaction, Chem. Asian J. 12 (2017) 1043–1047.
[22] Q.L. Ke, T.J. Sun, X.L. Wei, Y. Guo, S.D. Wang, Enhanced trace carbon dioxide capture on heteroatom-substituted RHO zeolites under humid conditions, ChemSusChem 10 (2017) 4207–4214.
[23] M. Palomino, A. Corma, F. Rey, S. Valencia, New insights on CO_2-methane separation using LTA zeolites with different Si/Al ratios and a first comparison with MOFs, Langmuir 26 (2010) 1910–1917.
[24] T.D. Pham, Q. Liu, R.F. Lobo, Carbon dioxide and nitrogen adsorption on cation-exchanged SSZ-13 zeolites, Langmuir 29 (2013) 832–839.
[25] L. Grajciar, J. Cejka, A. Zukal, C.O. Arean, G.T. Palomino, P. Nachtigall, Controlling the adsorption enthalpy of CO_2 in zeolites by framework topology and composition, ChemSusChem 5 (2012) 2011–2022.
[26] M.M. Lozinska, J.P.S. Mowat, P.A. Wright, S.P. Thompson, J.L. Jorda, M. Palomino, S. Valencia, F. Rey, Cation gating and relocation during the highly selective “trapdoor” adsorption of CO_2 on univalent cation forms of zeolite RHO, Chem. Mater. 26 (2014) 2052–2061.
[27] A. Medek, J.S. Harwood, L. Frydman, Multiple-quantum magic-angle spinning NMR: a new method for the study of quadrupolar nuclei in solids, J. Am. Chem. Soc. 117 (1995) 12779–12787.
[28] J.E. Schmidt, D. Fu, M.W. Deem, B.M. Weckhuysen, Template-framework interactions in tetraethylammonium-directed zeolite synthesis, Angew. Chem. Int. Ed. 55 (2016) 16044–16048.
[29] S. Araki, Y. Kiyohara, S. Tanaka, Y. Miyake, Crystallization process of zeolite RHO prepared by hydrothermal synthesis using 18-crown-6 ether as organic template, J. Colloid Interface Sci. 376 (2012) 28–33.
[30] A. Malek, G.A. Ozin, P.M. Macdonald, Probing cation sites in cesium-exchanged zeolite Y via ^{133}Cs MAS NMR, J. Phys. Chem. 100 (1996) 16662–16666.
[31] F. Yagi, N. Kanuka, H. Tsuji, S. Nakata, H. Kita, H. Hattori, ^{133}Cs and ^{23}Na MAS NMR studies of zeolite X containing cesium, Micropor. Mater. 9 (1997) 229–235.
[32] Y. Kim, R.J. Kirkpatrick, R.T. Cygan, ^{133}Cs NMR study of cesium on the surfaces of kaolinite and illite, Geochim. Cosmochim. Acta 60 (1996) 4059–4074.
[33] H. Koller, B. Burger, A.M. Schneider, G. Engelhardt, J. Weitkamp, Location of Na^+ and Cs^+ cations in CsNaY zeolites studied by ^{23}Na and ^{133}Cs magic-angle spinning nuclear magnetic resonance spectroscopy combined with X-ray structure analysis by rietveld refinement, Micropor. Mater. 5 (1995) 219–232.
[34] M. Hunger, U. Schenk, A. Buchholz, Mobility of cations and guest compounds in cesium-exchanged and impregnated zeolites Y and X investigated by high-temperature MAS NMR spectroscopy, J. Phys. Chem. B 104 (2000) 12230–12236.
[35] A. Nearchou, A. Sartbaeva, Influence of alkali metal cations on the formation of zeolites under hydrothermal conditions with no organic structure directing agents, Crystengcomm 17 (2015) 2496–2503.
[36] B.R. Cherry, M. Nyman, T.M. Alam, Investigation of cation environment and framework changes in silicotitanate exchange materials using solid-state ^{23}Na, ^{29}Si and ^{133}Cs MAS NMR, J. Solid State Chem. 177 (2004) 2079–2093.
[37] V. Laperche, J.F. Lambert, R. Prost, J.J. Fripiat, High-resolution solid-state NMR of exchangeable cations in the interlayer surface of a swelling mica: sodium-23, cadmium-111, and cesium-133 vermiculities, J. Phys. Chem. 94 (1990) 8821–8831.
[38] B. Casal, P. Aranda, J. Sanz, E. Ruizhitzky, Interlayer adsorption of macrocyclic-compounds (crown-ethers and cryptands) in 2/1 phyllosilicates: II. Structural features, Clay Miner. 29 (1994) 191–203.
[39] J. Kim, A. Maiti, L.C. Lin, J.K. Stolaroff, B. Smit, R.D. Aines, New materials for methane capture from dilute and medium-concentration sources, Nat. Commun. 4 (2013).
[40] D. Saha, Z.B. Bao, F. Jia, S.G. Deng, Adsorption of CO2, CH4, N2O, and N2 on MOF-5, MOF-177, and zeolite 5A, Environ. Sci. Technol. 44 (2010) 1820–1826.
[41] F.E. Epiepang, J. Li, Y. Liu, R.T. Yang, Low-pressure performance evaluation of CO_2, H_2O and CH_4 on Li-LSX as a superior adsorbent for air prepurification, Chem. Eng. Sci. 147 (2016) 100–108.
[42] R. Krishna, Describing the diffusion of guest molecules inside porous structures, J. Phys. Chem. C 113 (2009) 19756–19781.
[43] M. Fischer, R.G. Bell, Identifying promising zeolite frameworks for separation applications: a building-block-based approach, J. Phys. Chem. C 117 (2013) 17099–17110.
[44] A.W. Burton, S.I. Zones, S. Elomari, The chemistry of phase selectivity in the synthesis of high-silica zeolites, Curr. Opin. Colloid Interface Sci. 10 (2005) 211–219.
[45] E.P. Ng, D. Chateigner, T. Bein, V. Valtchev, S. Mintova, Capturing ultrasmall EMT zeolite from template-free systems, Science 335 (2012) 70–73.
[46] K. Ding, A. Corma, J.A. Macia-Agullo, J.G. Hu, S. Kramer, P.C. Stair, G.D. Stucky, Constructing hierarchical porous zeolites via kinetic regulation, J. Am. Chem. Soc. 137 (2015) 11238–11241.
[47] Y. Guo, T.J. Sun, X.W. Liu, Q.L. Ke, X.L. Wei, Y.M. Gu, S.D. Wang, Cost-efficiently synthesize CHA zeolites with controllable morphology and size by dual template – directed strategy, Chem. Eng. Sci. 358 (2019) 331–339.
[48] D.M. D'Alessandro, B. Smit, J.R. Long, Carbon dioxide capture: prospects for new materials, Angew. Chem. Int. Ed. 49 (2010) 6058–6082.
[49] P. Nugent, Y. Belmabkhout, S.D. Burd, A.J. Cairns, R. Luebke, K. Forrest, T. Pham, S.Q. Ma, B. Space, L. Wojtas, M. Eddaoudi, M.J. Zaworotko, Porous materials with optimal adsorption thermodynamics and kinetics for CO_2 separation, Nature 495 (2013) 80–84.
[50] K. Kordesch, V. Hacker, J. Gsellmann, M. Cifrain, G. Faleschini, P. Enzinger, R. Fankhauser, M. Ortner, M. Muhr, R.R. Aronson, Alkaline fuel cells applications, J. Power Sources 86 (2000) 162–165.
[51] J.C. Santos, F.D. Magalhaes, A. Mendes, Contamination of zeolites used in oxygen production by PSA: effects of water and carbon dioxide, Ind. Eng. Chem. Res. 47 (2008) 6197–6203.
[52] R. Krishna, S. Calero, B. Smit, Investigation of entropy effects during sorption of mixtures of alkanes in MFI zeolite, Chem. Eng. J. 88 (2002) 81–94.
[53] R. Krishna, J.M. van Baten, Using molecular simulations for screening of zeolites for separation of CO_2/CH_4 mixtures, Chem. Eng. J. 133 (2007) 121–131.
[54] M.R. Hudson, W.L. Queen, J.A. Mason, D.W. Fickel, R.F. Lobo, C.M. Brown, Unconventional, highly selective CO_2 adsorption in zeolite SSZ-13, J. Am. Chem. Soc. 134 (2012) 1970–1973.
[55] T.D. Pham, M.R. Hudson, C.M. Brown, R.F. Lobo, Molecular basis for the high CO_2 adsorption capacity of chabazite zeolites, ChemSusChem 7 (2014) 3031–3038.